\$ SOURCE BELSEVIER

Contents lists available at ScienceDirect

Earth and Planetary Science Letters

www.elsevier.com/locate/epsl



Sequences of seismic and aseismic slip on bimaterial faults show dominant rupture asymmetry and potential for elevated seismic hazard



Mohamed Abdelmeguid*, Ahmed Elbanna

Department of Civil and Environmental Engineering, University of Illinois at Urbana-Champaign, Urbana, IL 61801, United States of America

ARTICLE INFO

Article history: Received 13 December 2021 Received in revised form 21 May 2022 Accepted 25 May 2022 Available online xxxx Editor: R. Bendick

Keywords: bimaterial interfaces sequence of seismic and aseismic slip rupture asymmetry seismic hazard

ABSTRACT

We perform numerical simulations of sequences of earthquake and aseismic slip on planar rate and state faults separating dissimilar material within the 2-D plane strain approximation. We resolve all stages of the earthquake cycle from aseismic slip to fast ruptures while incorporating full inertia effects during seismic event propagation. We show that bimaterial coupling results in favorable nucleation site and subsequent asymmetric rupture propagation. We demonstrate that increasing the material contrast enhances this asymmetry leading to higher slip rates and normal stress drops in the preferred rupture propagation direction. The normal stress drop, induced by the bimaterial effect, leads to strong dynamic weakening of the fault and may destabilize the creeping region on a heterogeneous rate and state fault, resulting in extended rupture propagation. Such rupture penetration into creeping patches may lead to more frequent opening of earthquake gates, causing increased seismic hazard. Furthermore, bimaterial coupling may lead to irregular seismicity pattern in terms of event length, peak slip rates, and hypocenter location, depending on the properties of the creeping patches bordering the seismogenically active part of the fault. Our results highlight robust characteristics of bimaterial interfaces that persist over long sequence of events and suggest the need for further exploration of the role of material contrast in earthquake physics and models of seismic hazard.

© 2022 Elsevier B.V. All rights reserved.

1. Introduction

Contrast in elastic material properties across fault surfaces is not uncommon. Examples include strike-slip faults across different rock formations with variable material properties in contact with one another (Allam et al., 2014), crustal fault zones that have accumulated more damage on one side of the principal slip surface than the other one (Ben-Zion et al., 2003), subduction zones ioining continental and oceanic crustal blocks, and glaciers interfacing ice and underlying bedrock (Weertman, 1980; Danesi et al., 2007). Existence of such bimaterial interfaces has been confirmed by seismic imaging studies based on body waves (Eberhart-Phillips and Michael, 1998; Fuis et al., 2003; Shapiro, 2005; Thurber et al., 2004) as well as head waves (Ben-Zion and Malin, 1991; McGuire and Ben-Zion, 2005; Ben-Zion et al., 1992). The contrast in seismic velocities across fault surfaces may range between less than 5%, as in some strike slip faults, to more than 30%, as in some subduction zones (DeDontney et al., 2011a). For example, Fuis et al. (2003) identified a wave speed contrast of 1.09 for the San Andreas fault. For subduction zones, studies for velocity structure in Nankai, show a pressure wave speed contrast of 25%, and a shear wave speed contrast of 45% (Takahashi et al., 2002).

Prior theoretical work indicates that mode II ruptures along a frictional bimaterial interface between linear elastic solids produce dynamic changes of normal stress on the fault that depend on the slip rate function, material properties, and direction of rupture propagation (Weertman, 1980; Andrews and Ben-Zion, 1997; Adams, 1995; Ben-Zion, 2001; Ranjith and Rice, 2001). A sub-Rayleigh rupture propagating in the direction of slip on the compliant side of the fault causes a dynamic reduction of normal stress behind the rupture tip, whereas a rupture propagating in the opposite direction experiences a dynamic increase of normal stress behind the rupture tip. While the shear stress changes associated with slip grow like the Hilbert transform of the fault-parallel slip gradient, the magnitude of the normal stress changes is proportional to the slip gradient directly. Specifically, normal stress changes increase with the degree of material contrast across the fault, up to the largest contrast for which the generalized Rayleigh wave speed CGR exists, which is the case up to shear wave speed contrast of up to 30-40% for the range of material properties of common rock types.

^{*} Corresponding author.

E-mail address: meguid@illinois.edu (M. Abdelmeguid).

Experimental work has also been carried out to investigate dynamic rupture propagation along bimaterial interfaces. Anooshehpoor and Brune (1999) performed sliding experiments with two different foam rubber blocks and confirmed that large ruptures propagate in the theoretically predicted preferred direction alongside with the generation of Wrinkle-like slip pulse. Xia et al. (2004) performed sliding experiments along a bimaterial interface for several loading configurations and obtained asymmetric bilateral ruptures. Shlomai et al. (2016, 2020) studied the onset of frictional instability on bimaterial interfaces and the structure of the slip pulse with a focus on supershear rupture propagation.

McGuire et al. (2002) and Henry and Das (2001) analyzed rupture properties of over 100 large global earthquakes and found that most are predominantly unilateral. High-resolution locations of numerous small events on the San Andreas fault show a directional asymmetry that is compatible with a preferred propagation direction associated with the local velocity structure (Rubin and Gillard, 2000). Dor et al. (2006a, 2006b) mapped rock damage at several scales, ranging from 1 to 100 m, in the structures of several faults in southern California including the San Andreas, Punchbowl and San Jacinto faults. The results show considerably more damage on the crustal blocks that have faster seismic velocities based on available velocity models (Fuis et al., 2003; Shapiro, 2005; Lewis and Ben-Zion, 2010; Price and Scott, 1994; Lutter, 2004), consistent with the theoretical and numerical predictions of asymmetric damage formation about bimaterial interfaces. However, in a study of 450 small earthquakes at Parkfield, Kane et al. (2013) showed a roughly equal number of events propagating to the SE and NW and only saw greater rupture directivity in the preferred direction (70% SE) if they limited their data sets to those earthquakes of larger magnitudes. Similarly, through the inversions of spectral ratios of microearthquakes on the San Andreas fault, Wang and Rubin (2011) identified that while 40% of the earthquakes were bilaterial nearly twice as many had longer propagation in SE direction; additionally, they noted faster rupture velocities in SE direction. The issue of rupture directivity and asymmetry is still a debatable one (Harris and Day, 2005; Ben-Zion, 2006; Harris and Day, 2006).

Many numerical studies of dynamic ruptures have shown that the presence of bimaterial properties leads to a preferred rupture direction as well as asymmetric rupture features (sometimes propagating unilaterally), a preferred aftershock triggering and asymmetric off-fault damage (Ben-Zion and Shi, 2005; Ampuero and Ben-zion, 2008; Brietzke and Ben-Zion, 2006; Rubin and Ampuero, 2007; Duan, 2008; Dalguer and Day, 2009; DeDontney et al., 2011b). Particularly, these numerous studies gave insight into how rupture direction and rupture mode on bimaterial interfaces may be influenced by stress heterogeneity or co-seismic generation of off-fault plasticity. However, these conclusions rely on making apriori assumptions about the background stress and the nucleation procedure. It is thus unclear what part the bimaterial effect is robust over long sequence of seismic and aseismic slip that develop naturally with a smooth nucleation and self-consistent evolving prestress field.

To address this challenge, Erickson and Day (2016) numerically simulated a strike-slip fault governed by rate-and-state friction where quasi-dynamic events nucleate spontaneously due to remote, tectonic loading. They investigated the influence of material contrast over the course of many hundreds of years, and found that the presence of bimaterial properties, with contrasts ranging between 5-20%, influences the earthquake nucleation site, such that ruptures in the preferred direction are more favorable. For smaller values of the characteristic weakening distance in the rate and state friction law, partial ruptures that do not span the whole fault length may emerge. With material contrast present, some of these small events propagate in the non-preferred direction, enabled by

a favorable stress distribution left on the fault from previous rup-

While the work of Erickson and Day (2016) filled an important gap in the literature by being the first work, to the best of our knowledge, to study the bimaterial effect on earthquake cycles in a rate and state framework, it has important limitations. It neglected the effects of wave mediated stress transfer during seismic slip and approximated inertia by a radiation damping term limiting the investigation to the quasidynamic approximation. While prior work on earthquake cycle simulation has highlighted significant differences between quasidynamic and dynamic models (Thomas et al., 2014), including effects on peak slip rate, inter-event time, and event size distribution, inertia effects may be especially important for bimaterial interfaces as they directly influence the magnitude of the co-seismic normal stress changes which is central to the mechanics of rupture propagation.

Here we simulate sequence of earthquakes and aseismic slip on a strike slip fault governed by rate and state friction and separating two half spaces with different elastic properties using a recently developed methodology that resolves all stages of the earthquake cycle and incorporate full inertia effects during seismic rupture. We consider contrasts in the shear wave speeds of the two materials that range between 10% and 30%. The remainder of the paper is organized as follows Section 2 introduces the governing equations. Section 3 outlines the model setup and briefly introduces the numerical method considered here. In Section 4 we evaluate the role of bimaterial interfaces in altering the earthquake cycle pattern, including both aseismic and coseismic contributions, and role of varying the material contrasts. Finally, in Section 5, we conclude by discussing the implications of our results for source physics and seismic observations.

2. Governing equations

We consider the two-dimensional domain Ω undergoing plane strain deformations. The domain is divided into two half spaces by a planar strike-slip fault interface S_f . In the absence of body forces, the equation of motion for the 2-D plane strain problem is given by

$$\rho u_{\alpha,tt} = \sigma_{\alpha\beta,\beta} \quad \alpha, \beta = 1, 2 \quad \text{in} \quad \Omega$$
 (1)

with Dirichlet boundary conditions applied on the portion of the boundary denoted S_u and Neumann boundary conditions are applied on the portion of the boundary denoted S_T such that

$$u_{\alpha} = \bar{u}_{\alpha}$$
 on S_u (2)

$$\sigma_{\alpha\beta}n_{\beta} = \bar{\tau}_{\alpha} \quad \text{on} \quad S_T$$
 (3)

where u_{α} is the displacement vector, $\sigma_{\alpha\beta}$ is the stress tensor, ρ is material density, n_{β} is the outward normal vector (in 2-D) from the boundary. \bar{u}_{α} , and $\bar{\tau}$ are the prescribed displacements and tractions on the boundary surfaces S_u and S_T respectively. The stresses are given by the linear elastic constitutive law

$$\sigma_{\alpha\beta} = \lambda \delta_{\alpha\beta} \epsilon_{\gamma\gamma} + 2\mu \epsilon_{\alpha\beta} \tag{4}$$

where ε_{ij} is the strain tensor, and μ , and λ are the Lamé parameters, which may differ for each half space. Assuming infinitesimal deformations, the strain tensor is given by

$$\epsilon_{\alpha\beta} = \frac{1}{2} \left[u_{\alpha,\beta} + u_{\beta,\alpha} \right] \tag{5}$$

Frictional interface. On the fault surface S_f the tractions $T_{\alpha}^{\pm} = T_{\sigma,\alpha}^{\pm} + \Delta T_{\alpha}^{\pm}$, relative motion $[\![u_{\alpha}]\!]$, and relative velocity $[\![\dot{u}_{\alpha}]\!]$ are defined as:

$$\Delta T_{\alpha}^{\pm} = \Delta \sigma_{\alpha\beta}^{\pm} n_{\beta}^{\pm}, \quad \llbracket u_{\alpha} \rrbracket = (u_{\alpha}^{+} - u_{\alpha}^{-}), \quad \llbracket \dot{u}_{\alpha} \rrbracket = \frac{\partial \llbracket u_{\alpha} \rrbracket}{\partial t}$$
 (6)

Here, $T_{o,\alpha}^{\pm}$ is the initial traction and $\triangle T_{\alpha}^{\pm}$ is the change in traction due to fault slip, on either side of the fault surface. Imposing continuity conditions at the fault surface we obtain the following jump conditions and stress continuity conditions:

$$\llbracket u_1 \rrbracket = \delta, \quad \llbracket u_2 \rrbracket = \zeta \tag{7}$$

$$\Delta \sigma_{\alpha\beta}^{+} = \Delta \sigma_{\alpha\beta}^{-} \tag{8}$$

where, δ is the slip, and ζ is the fault opening. Additionally, to ensure no interpenetration we enforce that $\zeta \geq 0$. In subsequent sections, we will use V to denote the slipping velocity $\dot{\delta}$.

2.1. Rate-and-state friction

Here, we adopt a rate-and-state frictional (RSF) formulation used to describe friction in tectonic settings (Dieterich, 1979; Ruina, 1983). The boundary condition on the fault surface is enforced by equating the fault shear stress to its strength:

$$\tau = F(V, \theta) = f(V, \theta)\sigma_n \tag{9}$$

where the fault strength F is defined in terms of the effective normal stress σ_n and the friction coefficient f. In the RSF, the friction coefficient depends on the slip rate V and state θ as:

$$f(V,\theta) = f_0 + a \ln(V/V_0) + b \ln(\theta V/L) \tag{10}$$

where L is the characteristic slip distance, f_0 is the reference friction coefficient defined at a slip rate V_0 . The state evolution is prescribed through the aging law (Rice and Ruina, 1983), which is commonly used in earthquake cycle simulations (Lapusta et al., 2000; Erickson and Dunham, 2014; Herrendörfer et al., 2018; Liu and Rice, 2007) and defined as:

$$\frac{d\theta}{dt} = 1 - \frac{V\theta}{L} \tag{11}$$

This results in a steady-state solution of the state variable $\theta_{ss} = L/V$. The corresponding steady-state friction coefficient is given by:

$$f_{ss} = f_0 + (a - b) \ln \left(\frac{V}{V_0}\right) \tag{12}$$

Here, the parameter combination a-b>0 describes a steady state rate-strengthening frictional response and a-b<0 describes a steady state rate-weakening frictional response which can lead to unstable slip and stick slip sequences.

Rupture nucleation and process zone. RSF introduces a length scale for the nucleation size of earthquake that may be determined using an energy balance approach. Ampuero and Rubin (2008) established the following theoretical estimate for the nucleation size L_{nuc} for a frictional crack under slow tectonic loading:

$$L_{nuc} = \frac{2\mu^* Lb}{\pi \sigma_n (b-a)^2} \tag{13}$$

where, $\mu^* = \frac{1}{1-\nu}\mu$ for mode II rupture, μ is the shear modulus, and ν is Poisson's ratio. This nucleation size defines the critical wavelength that has to be resolved within the numerical scheme and is valid for a/b > 0.5. In addition to the nucleation size, Dieterich presented another characteristic length scale L_b , which is associated with the process zone during the propagation of the rupture when $V\theta/L >> 1$ and scales as b^{-1} (Dieterich, 1992). The quasi-static estimate for process zone L_b is given as:

$$L_b = \frac{\mu^* L}{\sigma_n b} \tag{14}$$

It is vital to properly resolve this length scale as it is more stringent than the nucleation zone's length. For dynamic simulations, continuously resolving the process zone becomes a more challenging ordeal as its size scales with the inverse of the Lorentz factor $\gamma_L(v_r) = \sqrt{1-v_r^2/c_s^2}$, where, v_r is rupture speed, and c_s is the shear wave speed. The Lorentzian contraction implies that the process zone will shrink with increasing rupture propagation speed v_r (Freund, 1979).

We further note, that for the case of a planar fault bisecting similar material, the effective normal stress remains constant in time $\sigma_n = \sigma_n^o$, thus we can readily estimate the nucleation size and the process zone through expressions (13) and (14) respectively. For the bimaterial case, the induced deformations introduce perturbations in the normal stress, which alters the computation of these length scales. To this end, and for the sake of representation, we normalize our results using L_{nuc}^H

$$L_{nuc}^{H} = \frac{2\mu_{H}^{*}Lb}{\pi \sigma_{n}^{0}(b-a)^{2}}$$
 (15)

This nucleation size is based on a homogeneous bulk with shear modulus μ_H and initial normal stress σ_n^o . We further note the effective rigidity of domain is another key parameter for estimating the nucleation length scale. An estimate of the reduction in nucleation size is computed through the modulus M which depends on the material properties of the two halfspaces and is proportional to material contrast r_c (Rice et al., 2001). The nucleation size then scales like $L_{nuc} \propto M/\mu_H^* L_{nuc}^H$ (Hutchinson and Suo, 1991).

Normal stress regularization. To account for rapid variations in normal stress that could occur due to the material mismatch, we utilize a RSF formulation featuring a delayed response of the shear stress according to Prakash-Clifton law. This model fits observed frictional response better than the traditional formulation (Cochard and Rice, 2000; Ranjith and Rice, 2001). In this framework, the fault strength is given by the following (Tal et al., 2020):

$$F = f(V, \theta)\xi \tag{16}$$

The function ξ evolves exponentially with slip to the new value of σ as

$$\dot{\xi} = \frac{-V}{L_{PC}}(\xi - \sigma_n) \tag{17}$$

where L_{PC} is an evolution distance of choice. In our time stepping, we consider this as an additional evolution equation to compute ξ at any given time. In our analysis, we utilized a proportional scaling of the evolution distance relative to the characteristic length of RSF, such that $L_{PC}=25L$. This allows for a sufficiently smooth variation in the frictional strength within the numerical framework, while not deviating substantially from the non-regularized version of RSF. We note that a different choice of L_{PC} could lead to either an enhanced bimaterial effect for smaller values L_{PC} or a diminished bimaterial effect for very high values of L_{PC} .

3. Model description

3.1. Model setup

We consider sequence of earthquakes and aseismic slip on a strike slip fault governed by rate-and-state friction in 2-D plan strain condition. The fault separates two dissimilar half-spaces shown in (Fig. 1a). On the fault, a potentially seismogenic patch borders regions steadily moving with a prescribed slip rate V_{pl} .

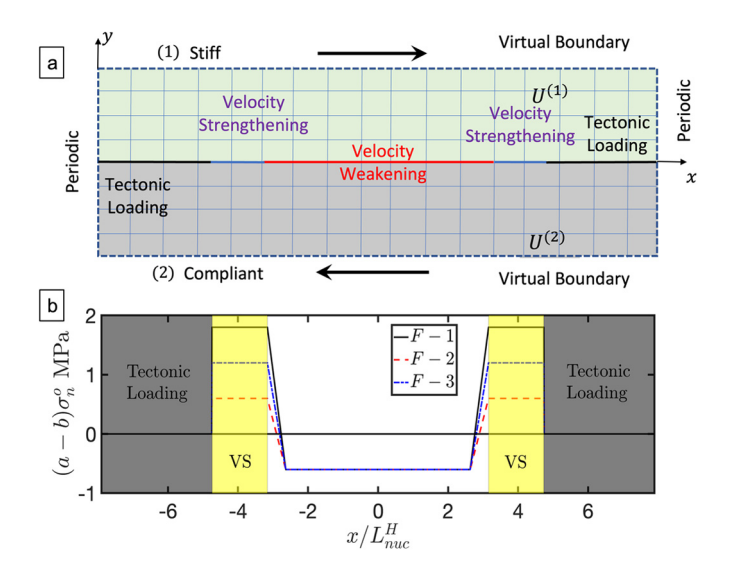


Fig. 1. Model Setup: A planar rate and state fault separates two elastic half spaces with dissimilar seismic velocities. (a) The computational setup for the hybrid FE-SBI scheme. The finite element method is used to discretize a small domain adjacent to the fault surface. The spectral boundary integral method is used to simulate the external half spaces without explicitly discretizing them by enforcing an integral relation between the slip and stresses on the virtual boundaries parallel to the fault surface. Periodic boundary conditions are used on the lateral boundaries of the domain. (b) Distribution of the fault frictional properties for three different cases of velocity strengthening patches.

Table 1Parameters description.

Medium Parameter	Symbol	Value
Shear wave speed (Stiff) (km/s)	c_s^1	3.464
Pressure wave speed (Stiff) (km/s)	c_p^1 c_p^2 c_p^2	6
Shear wave speed (Compliant) (km/s)	c_s^2	varies
Pressure wave speed (Compliant) (km/s)	c_p^2	varies
Density (kg/m ³)	$\stackrel{\cdot}{ ho}$	2670.0
Width of the domain (m)	W	150
Distance between two virtual boundaries (m)	W_s	2
Fault Parameters	Symbol	Value
Static Coefficient of friction	f_o	0.6
Critical slip distance (m)	L	10^{-4}
Reference velocity (m/s)	V_o	10^{-6}
Tectonic loading (m/s)	V_{pl}	10^{-9}
Width of VW patch (m)	\hat{W}_{VW}	50
Width of transition (m)	W_T	5
Width of the fault (m)	W_f	90
Initial Effective normal stress (MPa)	σ_n^o	120
Initial shear stress (MPa)	τ^{o}	58.8
Steady state velocity dependence in VW patch	$(a_{VW}-b)$	-0.005
Steady state velocity dependence in VS patch	$(a_{VS}-b)$	varies

The parameters used in the simulations are listed in Table 1. We consider different material contrasts r_c , defined as $r_c = c_s^2/c_s^1 = c_p^2/c_p^1$, where c_s and c_p are the shear and pressure wave speeds, respectively, and the superscripts refer to the two half spaces associated with a (1) stiff and (2) compliant medium. We define bimaterial models with a contrast ratio $r_c < 1$. Additionally, Fig. 1b shows the heterogeneous spatial distribution of friction parameters to create rheological transitions. Specifically, we consider the effect of the frictional properties of the creeping regions on the patterns of seismicity.

3.2. Numerical scheme

In our numerical model we utilize a coupled finite element and boundary element code FEBE to simulate sequence of earthquake and aseismic slip (SEAS) on a fault surface together with wave propagation in the adjacent medium. This approach was initially introduced to simulate spontaneous dynamic rupture propagation for 2-D inplane problems by Ma et al. (2018) and later extended to SEAS by Abdelmeguid et al. (2019) in anti-plane setting.

Spatial discretization. The coupling procedure between the two methods ensures that continuity is enforced at the interface S_S between the FE and BE domain through consistent communication of boundary conditions. This domain truncation approach allows for efficient, yet accurate modeling of the rupture propagation and complex fault zone properties. Accordingly, the FE portion of the domain includes all the material and geometrical complexities associated with the fault zone which is properly resolved as demonstrated in Ma and Elbanna (2019), and the homogeneous bulk is modeled using a BE approach known as spectral boundary integral method (SBIM) which is efficient and computationally inexpensive (Ma and Elbanna, 2019; Geubelle and Breitenfeld, 1997; Lapusta and Rice, 2003).

Temporal discretization. Instead of simulating the dynamic rupture propagation of a single earthquake that involves artificially overstressing the fault, we opt for a more self-consistent approach in which the entire sequence of earthquakes and aseismic slip is simulated. During the inter-seismic phase, aseismic slip is accumulated as the fault is stressed gradually through the background plate tectonic loading V_{pl} applied on the edges of the interface. The accumulation of aseismic slip result in stress concentration that spontaneously nucleate an earthquake consistent with the frictional law and material response. Here, we utilize a quasidynamic approximation during periods of aseismic slip and switch to fully dynamic approach during the dynamic rupture period. During the quasi-dynamic periods we utilize an adaptive time marching scheme (Lapusta et al., 2000). The time step during dynamic rupture periods is chosen to satisfy the CFL condition. This hybrid, quasi-dynamic-fully-dynamic, scheme is computationally efficient as it enables the choice of large time steps during periods of slow tectonic loading without compromising stability.

We switch between quasi-dynamic and fully dynamic solvers based on the value of the maximum slip rate. For the problem discussed below we switch from quasi-dynamic scheme to a dynamic scheme based on a threshold $V^{QD}=1$ mm/s, and from dynamic to quasi-dynamic based on a threshold $V^{DQ}=0.5$ mm/s. To evaluate the role of transition threshold, we estimate the ratio between radiation damping term given as ηV , where $\eta = \mu^{(1)} \mu^{(2)}/(c_s^{(1)} \mu^{(2)} + c_s^{(2)} \mu^{(1)})$ and quasi-static shear stress τ_{qs} . Neglecting the inertia effects is justifiable as long as the magnitude of the radiation damping term is relatively small which is ensured by having the ratio $R = \eta V/\tau_{qs}$ much smaller than unity R <<1. The above thresholds ensure that ratio $R <10^{-4}$. Furthermore, we have performed numerical tests to confirm that the accuracy of the obtained results is independent of the threshold choice, as long as it is small enough as outlined above.

4. Results

Slip on a planar bimaterial interface is fundamentally different from slip on a planar interface in a homogeneous bulk. In the bimaterial case, stress transfer between the two half-spaces couples local variations in the normal stress with interface slip. This coupling is independent of the frictional properties of the fault. Rather, it depends entirely on the elastic properties of the two half-spaces, namely, the material mismatch. Furthermore, the bimaterial coupling intensifies near the rupture tip. The sign of the coupling (i.e. whether it introduces compressive or tensile normal stress perturbation) depends on the rupture propagation direction with respect to the sense of motion in the more compliant medium. Here, we adopt the notion that a preferred direction refers to the rupture propagation in the direction of the more compliant material, Along

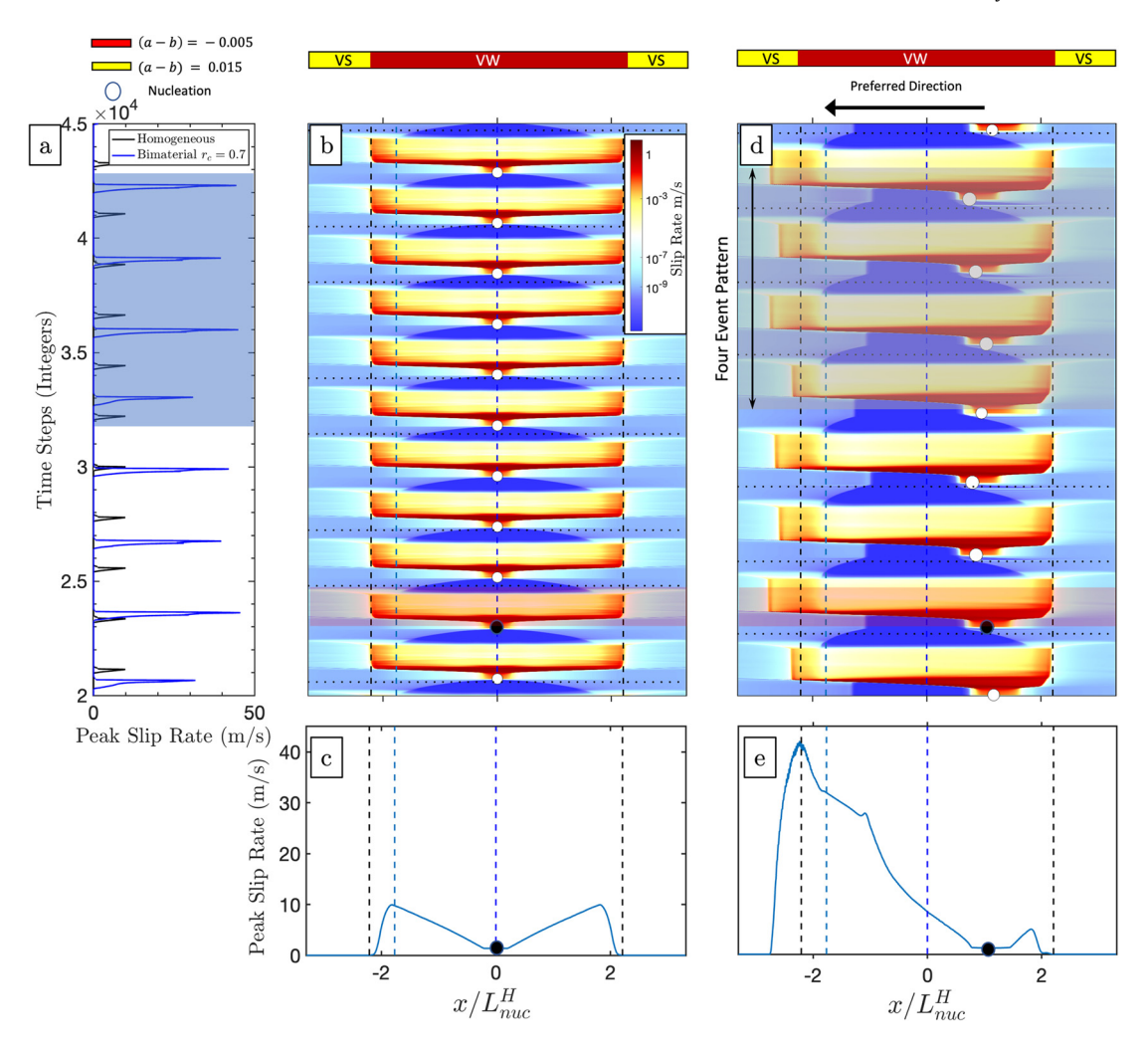


Fig. 2. Sequences of earthquakes and aseismic slip on a bimaterial interface versus an interface in a homogeneous medium. (a) Peak Slip rate. Material contrast across the frictional interface contributes to an increase in peak slip rate during the seismic events and subsequently larger slip accumulation. (b) Time history of the slip rate contours in the homogeneous case. The sequence of earthquakes is periodic and rupture propagates symmetrically on the fault surface. (c) Spatial distribution of maximum slip rate during a dynamic event for homogeneous case (hypocenter marked with black circle). (d) Time history of the slip rate contours on the bimaterial interface. The material contrast results in emergence of a preferred nucleation site, asymmetric rupture propagation, and irregular seismic pattern marked by periodic clusters rather than periodicity of individual events as in the homogeneous case. (e) Spatial distribution of maximum slip rate during a dynamic event for bimaterial case (hypocenter marked with black circle). In the contour plots, the fault length is normalized by the nucleation size, time is given by simulation time steps, and the dashed black line indicates the onset of the creeping regions. The time steps could vary between the homogeneous and bimaterial cases and are not indicative of absolute time.

the preferred direction, normal stress decreases behind the rupture tip. In contrast, for the non-preferred direction, where the rupture propagation is in the direction of the stiffer medium particle motion, the normal stress increases behind the rupture tip.

4.1. Earthquake cycle on bimaterial interface

Here, we focus on the role of material mismatch on the overall behavior of the earthquake cycle, including its influence on rupture directivity, the complexity of earthquake sequence, and destabilization of stable creeping regions. We fix the frictional parameters of the rate weakening patch as we vary the shear wave speed c_s and pressure wave speed c_p of one half-space relative to the other one.

Fig. 2 shows the time history for slip rate comparing a homogeneous model (case (1)) to a bimaterial case with $r_c=0.7$ (case(2)). Fig. 2a shows the time history (time steps) of the peak slip rate for case (1) versus case (2). The introduction of material mismatch contributes to higher peak slip rates per event. As the rupture propagates in the preferred direction, tensile change in the normal stress introduces a dynamic weakening mechanism that favors the rupture propagation in that direction resulting in

higher slip rates than the homogeneous case. Fig. 2b,d illustrates the slip rate contours for both aseismic and co-seismic periods of the earthquake cycle. For the homogeneous case, shown in Fig. 2b the problem is symmetric about the center point of the fault x = 0. Fig. 2c shows the spatial distribution of the peak slip rate for a single dynamic rupture event (hypocenter marked with black circle) further emphasizing the symmetric nature of the propagating rupture. However, for the bimaterial interface, the coupling between normal stress and fault slip result in asymmetric stress distribution during inter-seismic creep which dictates the nucleation site of the rupture. Specifically, the nucleation site for the bimaterial case is shifted towards the right end of the fault. We observe for the homogeneous case (Fig. 2b) the pattern of earthquakes is periodic with identical seismic events and that the nucleation site remains the same throughout the whole time series. Furthermore, the spatial distribution of peak slip rate during dynamic rupture shown in Fig. 2e highlights the asymmetric nature of rupture propagation on bimaterial interfaces. Particularly, we observe that the peak slip is substantially higher for the rupture front propagating in the preferred direction.

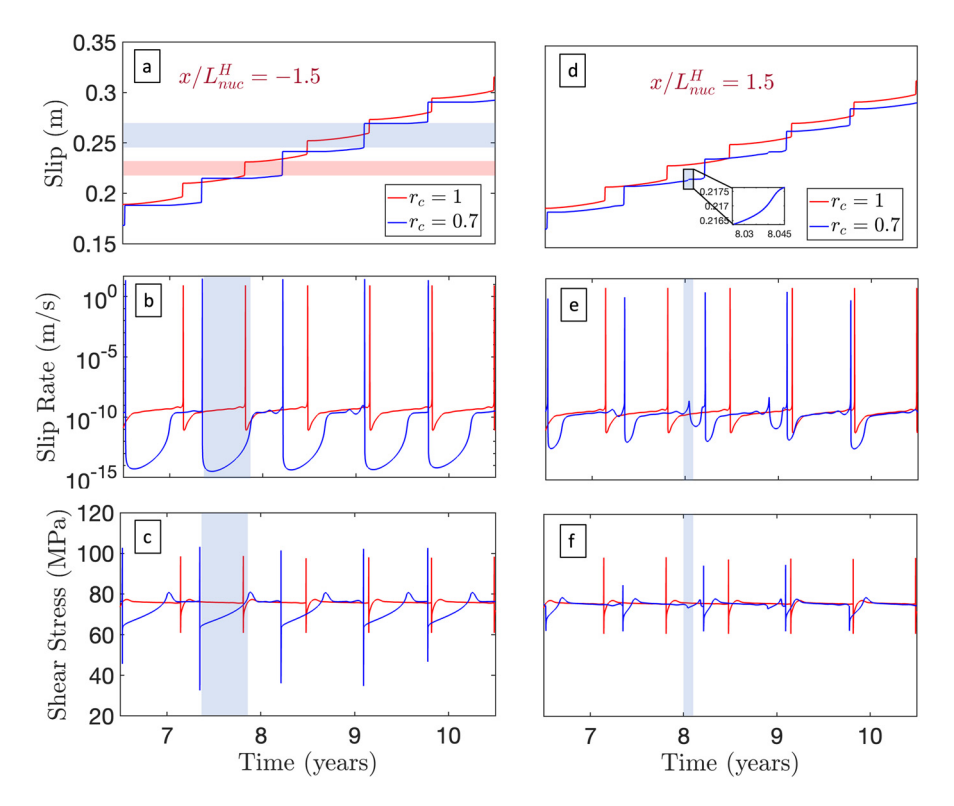


Fig. 3. A comparison of rupture characteristics between a bimaterial interface and an interface bisecting a homogeneous medium. (a) time history of the slip shown at $x/L_{nuc}^H = -1.5$ corresponding to point located in the preferred direction of propagation in the bimaterial sense (slip accumulation for bimaterial interface is highlighted in blue and slip accumulation for homogeneous case is highlighted in red). (b) time history of the slip rate shown at $x/L_{nuc}^H = -1.5$ corresponding to point located in the preferred direction of propagation in the bimaterial sense (post-seismic locking is highlighted in blue). (c) time history of the shear stress shown at $x/L_{nuc}^H = -1.5$ corresponding to point located in the preferred direction of propagation in the bimaterial sense (post-seismic locking is highlighted in blue). (d) time history of the slip shown at $x/L_{nuc}^H = 1.5$ corresponding to point located in the non-preferred direction (accelerated slip jumps are highlighted in blue). (e) time history of the slip rate shown at $x/L_{nuc}^H = 1.5$ corresponding to point located in the preferred direction of propagation in the bimaterial sense (accelerated slip jumps are highlighted in blue). (f) time history of the shear stress shown at $x/L_{nuc}^H = 1.5$ corresponding to point located in the non-preferred direction of propagation in the bimaterial sense (accelerated slip jumps are highlighted in blue). (For interpretation of the colors in the figure(s), the reader is referred to the web version of this article.)

In contrast, the introduction of material mismatch as shown Fig. 2d perturb the earthquake cycle periodicity and lead to several quantitative differences including:

- 1. Nucleation: For the bimaterial case, ruptures preferably nucleate on the right half of the fault and propagate towards the left in the preferable direction. There is some variability in the hypocenter locations due to the stress heterogeneity that evolve from one event to another.
- 2. Peak slip rate: the introduction of bimaterial interface results in an increase in the peak slip rate in comparison with the homogeneous model. Furthermore, within the earthquake sequence various events emerge with different peak slip rates.
- 3. Earthquake pattern: while the homogeneous case resulted in periodic events, the introduction of material mismatch contributed to the emergence of clusters where a four-event pattern repeats throughout the earthquake cycle. The onset of the four-event pattern is marked by an event with smaller peak slip rate followed by three larger events with higher peak slip rate.
- 4. Rupture penetration in the creeping region: we observe that with the introduction of the bimaterial interface rupture front propagating within the preferred direction produces sufficient normal stress perturbations to destabilize the velocity strengthening patch. Instead of arresting at the boundary of the stable velocity strengthening patch, as in the homogeneous case, the rupture extends beyond the rate weakening portion of the fault. The extent of the rupture penetration varies from one event to another within the four event pattern (highlighted in Fig. 2c)

To gain further insight on the role of the material mismatch we consider the time history evolution of slip, slip rate, and shear stress at different points $x/L_{nuc}^H = -1.5$, and 1.5 along the fault, comparing the homogeneous case and a bimaterial case. For the bimaterial case, $x/L_{nuc}^H = -1.5$ coincide with preferred direction properties. rection propagation. Fig. 3a shows the slip evolution in time at $x/L_{nuc}^{H} = -1.5$. Co-seismically, a bimaterial interface yields higher slip accumulation (highlighted in blue) when compared to the homogeneous case (highlighted in red) due to directivity of rupture propagation. In contrast, aseismic slip accumulation on a bimaterial interface is negligible at point $x/L_{nuc}^H=-1.5$ in which the slip rate drops substantially when compared to the homogeneous case at the same location as shown in Fig. 3b. The substantial deceleration is mainly attributed to the higher shear stress drop carried by the rupture front propagating in the preferred direction. Fig. 3c shows that indeed following the dynamic rupture, the shear stress on the bimaterial interface is substantially lower leading to a near locking of the fault surface. Furthermore, the slip rates for a bimaterial interface are inherently larger as demonstrated in Fig. 3b due to the enhanced dynamic weakening effect arising from the coupling between the changes in normal stress and fault slip in the preferred direction

In the non-preferred direction $x/L_{nuc}^H=1.5$ we observe similarities between the bimaterial and the homogeneous cases in terms of slip accumulation during both coseismic and aseismic periods as shown in Fig. 3d. Interestingly we observe small sudden accumulation (highlighted in blue and in the zoomed in figure) of slip during aseismic periods. Fig. 3e-f elaborates further on this behavior as we observe aseismic accelerations $V \sim 1e^{-8}$ (highlighted in blue) and stress drops prior to the large event occurrences

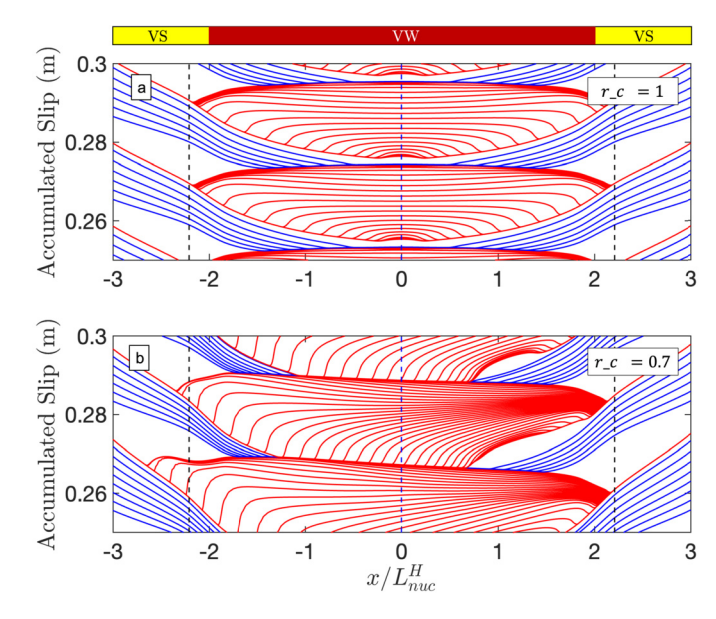


Fig. 4. A comparison of slip accumulation on the bimaterial interface vs slip accumulation on an interface in a homogeneous medium. Slip during aseismic period (blue) is plotted every 0.1 yr. Slip during the coseismic period (red) is plotted every 0.001 s. (a) Slip contours for the homogeneous case showing rupture arrest at the boundaries of the creeping region. (b) Slip contours for the bimaterial case showing rupture penetration into the creeping, velocity strengthening, region in the preferred direction and rupture arrest at the rheological boundary in the non-preferred direction.

that are absent from the homogeneous case. We note that the time between the previous event and this small scale instability is $T_c = 0.672$ yr, which is very similar to the recurrence time for the earthquake events on the homogeneous interface. This suggests that the occurrences of these instabilities are tied with an unsuccessful attempt for nucleation on the creeping front. Specifically, the local stress state may initiate the nucleation process, however the average stress state on the fault, resulting from prior events, may cause the arrest of the emerging instabilities. This highlights the important role of emerging heterogeneous stress distribution in regulating slip instabilities.

Fig. 4a-b shows the slip accumulation during a portion of the earthquake sequence representing the aseismic slip (blue) plotted every 0.1 yr and the coseismic slip (red) plotted every 0.001 seconds. For the homogeneous case a periodic structure of events emerge as demonstrated in Fig. 4a. Fig. 4b for the bimaterial case, highlights two crucial observations: (1) Slip accumulation in the preferred direction of propagation increases with rupture propagation distance. (2) Dynamic slipping of the stable creeping patch in the preferred direction of propagation suggesting a destabilization effect that is absent in the homogeneous case. The dynamic rupture penetrates within the VS region beyond the extent of the rate weakening patch. This penetration is facilitated by the tensile normal stress perturbation emerging from the coupling between slip and normal stress changes in the preferred direction. While the penetration is initially accompanied by a transient slip deceleration localized at the boundary of the velocity strengthening region, the spacing of the slip lines within that region suggests that the dynamic rupture maintains approximately its speed as it penetrates through the VS region until the rupture is eventually arrested.

4.2. Dynamic weakening

The rupture penetration shown in Fig. 2c and 4b into creeping patch is attributed to bimaterial coupling and subsequent dynamic weakening that occurs as the rupture propagates within the preferred direction. To explore this behavior further, Fig. 5a shows

the evolution of shear stress versus slip for eighth event in the cycle (highlighted in Fig. 3b) at two locations $x/L_{nuc}^H=1.5$, and $x/L_{nuc}^H=-1.5$. The clear signature of the dynamic weakening in the bimaterial case is highlighted, in which the shear stress drops significantly during coseismic rupture due to the bimaterial coupling in the preferred direction. The dynamic weakening behavior further contributes to the lack of aseismic slip accumulation, and longer inter-seismic periods as shown in Fig. 3a-b.

Similarly, the weakening effect is further emphasized in Fig. 5b showing evolution of shear stress versus the slip rate. This dynamic strength reduction in the preferred direction of propagation is the result of rapid normal stress changes carried by the rupture tip due to the bimaterial coupling effect. This observed weakening of the fault strength is carried forward into the creeping patch as rupture continues to propagate in the preferred direction, and predominately contributes to the destabilization of velocity strengthening portion of the fault. Rupture arrest occurs when the dynamic weakening effects from the rupture propagation in the preferred direction can no longer sustain the propagation.

4.3. Role of material contrast

To evaluate the role of different material contrasts, we simulate two intermediate contrast ratios corresponding to case (1) $r_c = 0.9$ and case (2) $r_c = 0.8$ commonly observed in strike-slip faults. Fig. 6a-b shows the slip rate contours evolution for the time period between 6.5 and 10.5 yr. We note that the nucleation size decreases with an increase in material contrast. This is because for a bimaterial interface the effective shear modulus of the medium is reduced due to the existence of a more compliant half space. This in turn reduces the nucleation size which is proportional to the effective rigidity. As discussed in Section 2.1 an estimate of the reduction in nucleation size is computed through the modulus M which depends on the material properties of the two halfspaces and is proportional to material contrast r_c (Rice et al., 2001). The nucleation size then scales like $L_{nuc} \propto M/\mu_H^* L_{nuc}^H$ (Hutchinson and Suo, 1991). For $r_c = 0.9$ the modulus ratio $M/\mu_H^* = 0.9$, while for $r_c = 0.8$ the modulus ratio $M/\mu_H^* = 0.78$

Furthermore, Fig. 6c compares the peak slip rate for the two sampled events (I), and (II) (highlighted in the figure). The peak slip rate increases from $V \sim 25$ (m/s) to $V \sim 34$ (m/s) as the contrast in wave speed increases. This behavior may be explained by considering the following estimate for slip rate based on dimensional analysis $V \propto \Delta \tau v_r / \tilde{\mu}$, where v_r is the rupture speed, $\Delta \tau$ is the stress drop, and $\tilde{\mu}$ is the effective shear modulus. Both the rupture speed and the stress drop increase as the material contrast is increased. The effective shear modulus decreases as the material contrast is increased. Thus, the combination of these parameters leads to higher peak slip rates. Finally, the recurrence interval between earthquakes also increased from 0.72 to 0.75 yr as the material contrast increase. Qualitatively, this maybe be explained as follows. Assuming a constant stress drop $\Delta \tau$ and stressing rate $\dot{\tau}$, the recurrence interval is $T_c \propto \Delta \tau / \dot{\tau}$. Fig. 3 shows that the stress drop increases with the introduction of bimaterial interface. Similarly, the stressing rate drops due to the reduction in effective rigidity. Consequently, the inter-event time increases with increasing material contrast.

The drop in the normal stress in the preferred direction of propagation, shown in Fig. 6d for the sampled events (I), and (II) (highlighted in Fig. 6e), increase with material contrast as well as propagation distance from the nucleation site. This increased reduction in normal stress contributes to the slightly extended rupture propagation distance seen in Fig. 6a-b. We expect this effect to be amplified on longer faults where the rupture has the opportunity to propagate for larger distances and, hence, experience stronger reduction in the normal stress.

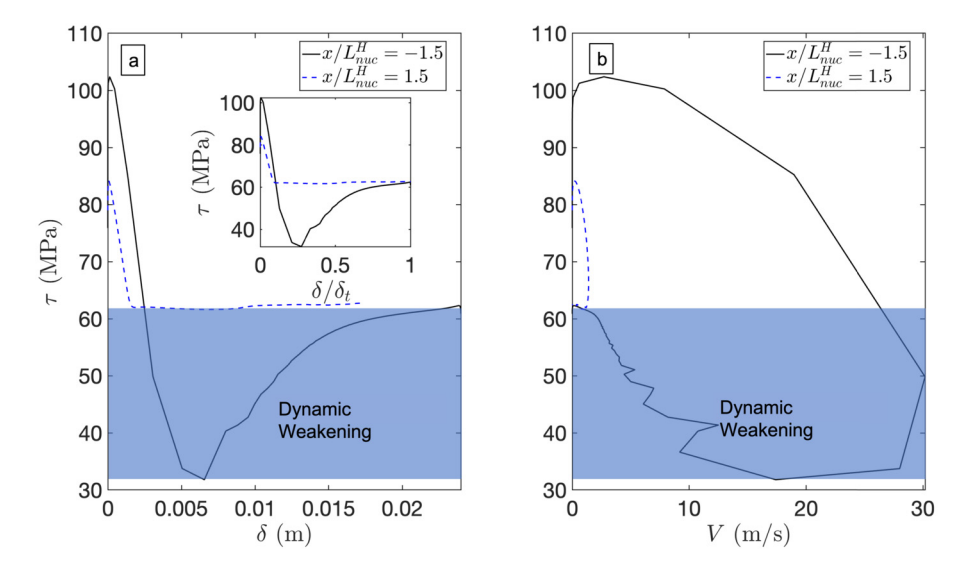


Fig. 5. Dynamic weakening of bimaterial interfaces. (a) Shear stress evolution versus slip at $x/L_{nuc}^H = -1.5$, and $x/L_{nuc}^H = 1.5$ For x/L = -1.5, a point in the preferred direction, there is a significant drop in the shear stress followed by gradual recovery highlighted in the shaded region. For $x/L_{nuc}^H = 1.5$, a point in the non-preferred direction, the shear stress initially drop but remains steady at a value higher than what is observed for $x/L_{nuc}^H = -1.5$ suggesting little dynamic weakening. The insert replicates the stress slip curves but with the slip in each case normalized by the total slip accumulated at the point. (b) Shear stress evolution versus slip rate at $x/L_{nuc}^H = -1.5$, and $x/L_{nuc}^H = 1.5$ for a bimaterial interface during event eight showing strong rate weakening response for the frictional interface in the preferred direction of propagation and limited rate weakening in the non-preferred direction.

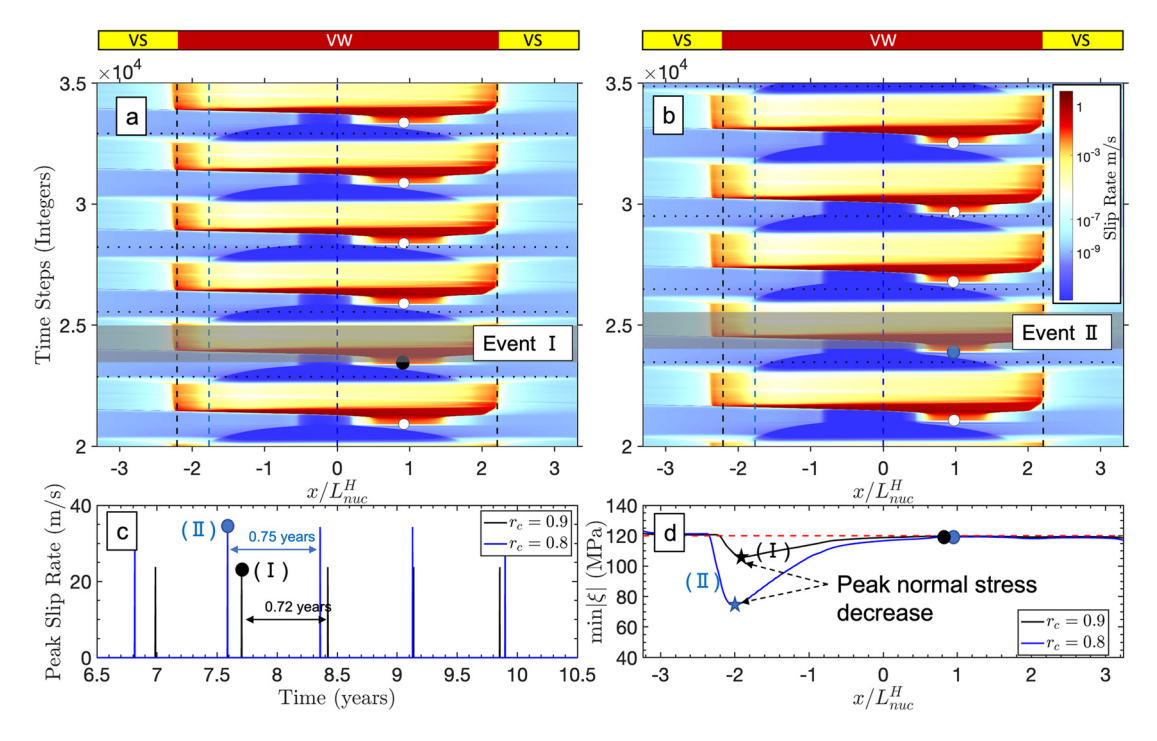


Fig. 6. Sequence of earthquakes and aseismic slip on a bimaterial interface for different material contrasts. (a) Slip rate contours for material contrast $r_c = 0.8$. The nucleation length is highlighted for both contrasts. (c) Peak slip rate plot for the time period between 5 and 8 yr comparing different material contrast. Events (I) and (II) are highlighted and referred to in (a), and (b). (d) Distribution of the minimum regularized normal stress as a function of position on the fault for events (I) and (II).

4.4. Normal stress variation

We explore the dependence of the normal stress perturbation on the slip rate. Fig. 7 illustrates the change in normal stress drop due to changes in the peak slip rate, we observe that at a given material contrast the normal stress drop increases linearly with the peak slip rate $\Delta \xi \propto C'V$. The slope C' depends on the material contrast of the model (as shown in Fig. 7). This observation is consistent with the theoretical results for a steadily propagat-

ing dislocation (Weertman, 1980; Andrews and Ben-Zion, 1997), in which the normal traction is also linearly proportional to the slip rate $\sigma_n = \tilde{\mu} V/v_r$, where, $\tilde{\mu}$ is an algebraic function of the material properties and rupture velocity v_r (Weertman, 1980), which plays the role of an effective elastic modulus. This observation further suggests that the bimaterial effect may dominate the response of long enough faults since slip rate generally increases with propagation distance, at least until the rupture saturates the seismogenic depth.

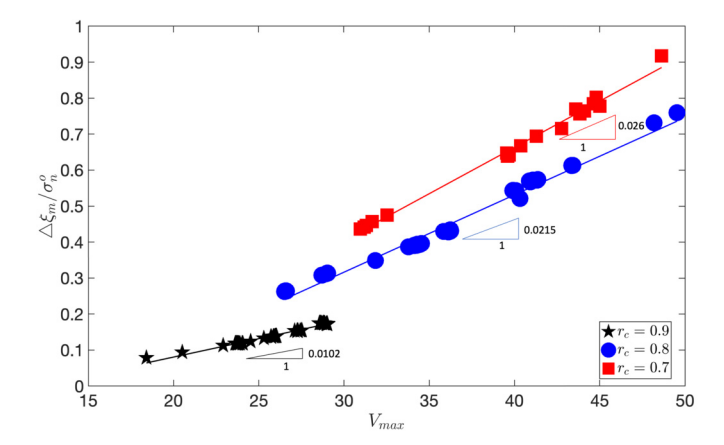


Fig. 7. Correlation between normal stress changes and slip rate. Maximum normal stress drop increases linearly with the peak slip rate with the slope dependent on the material contrast.

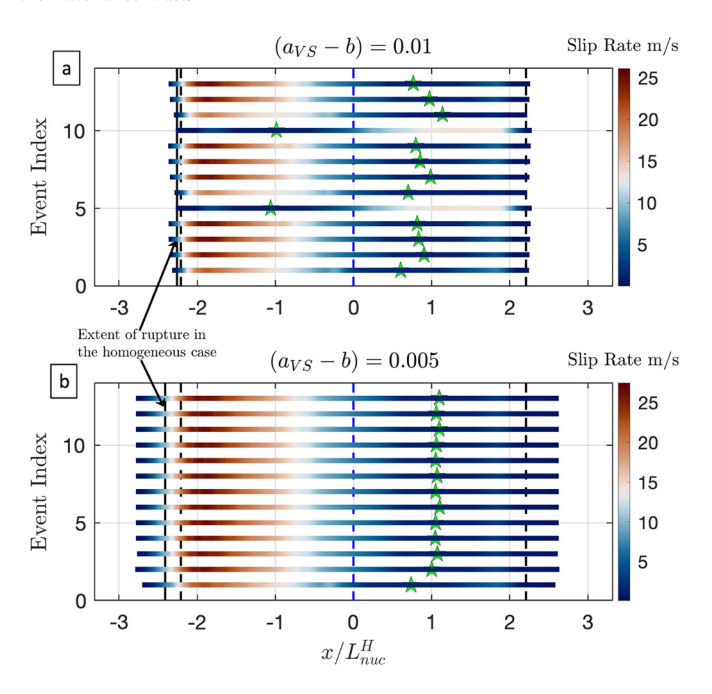


Fig. 8. The role of frictional properties of the creeping (velocity strengthening) regions in modulating sequence of earthquakes and aseismic slip on a bimaterial interface. (a) Seismic events pattern for $(a_{VS}-b)=0.01$ and (b) Seismic events pattern for $(a_{VS}-b)=0.005$. Each line represents the extent of a seismic event. The star indicates the nucleation site of the event. The shading on each line indicates the maximum slip rate at that position during the dynamic rupture. See text for discussion.

4.5. Rupture penetration into the creeping region

In the presence of a bimaterial interface the interaction between normal stress perturbations and the frictional properties of the velocity strengthening patch alters the patch resistance to slip, and may consequently influence the earthquake sequence. Mainly, as mentioned earlier, the coupling between slip and normal stress perturbations could have a destabilization impact enabling rupture penetration within the velocity strengthening patch. This increases seismic risk, by enabling the rupture to propagate longer, and also affects subsequent event dynamics, by influencing the post-event stress distribution. To study this interaction we focus on a specific material contrast $r_c = 0.9$ and vary the frictional properties of the VS region. In addition to the case (1) $(a_{VS} - b) = 0.015$ presented in the previous section, we consider case (2) where $(a_{VS} - b) = 0.01$, and case (3) $(a_{VS} - b) = 0.005$ the choice of pa-

rameters indicates a reduction in the fault strengthening behavior within the creeping region since $\Delta f_{ss} = (a-b) \ln(V/V_o)$. For case (2) with $(a_{VS}-b)=0.01$ Fig. 8a demonstrate the extent of the rupture propagation marked by the maximum slip rate contours along the bimaterial interface. The results suggest a larger rupture length due to slip penetration beyond the rate weakening patch and into the rate strengthening region, whose boundary is marked in the figure by dotted black lines, compared to case (1) shown in Fig. 5a.

Furthermore, in case (2) $(a_{VS} - b) = 0.01$ (Fig. 8a) the earth-quake sequence pattern varies significantly by altering the frictional properties of the velocity strengthening patch. Particularly, we observe that the earthquake sequence is not entirely uniform, rather we obtain complexity in the distribution of the nucleation sites (represented by the green stars). Interestingly, for this particular choice of parameters the rupture may nucleate within the left half of the fault indicating that weakening of the velocity strengthening zone could alter the stress state on the fault enabling occasional rupture nucleation in non-preferred sites. The earthquake cycle, however, converged to a pattern of four ruptures propagating in the preferred direction and one rupture propagating predominately in the non-preferred direction. For this particular $a_{VS} - b$ value, the counterpart homogeneous case events remain symmetric about the center of the fault.

Fig. 8b shows the rupture extent for case (3) $(a_{VS} - b) = 0.005$ we observe that the rupture extent is increased further with deeper penetration in the preferred rupture direction. Unlike case (2), we do not observe nucleation of events that predominately propagate in the non-preferred direction. The slip contours indicate that peak slip rate in the preferred direction stays quite large V > 15 m/s as the front penetrates deeper within the creeping region relative to the extent of rupture propagation in the homogeneous domain highlighted in Fig. 8a-b prior to the eventual rupture arrest. The rupture front propagating in the non-preferred direction, however, maintains a lower slip rate due to the increased fault resistance in that direction.

To explore the rupture penetration further, Fig. 9a shows the extent of rupture penetration L_{pen} for various cases of $(a_{VS} - b)$ and material contrasts. For a homogeneous case we observe that the rupture may also penetrate into the velocity strengthening patch as $(a_{VS} - b)$ decreases due to the reduction in patch resistance. The inclusion of a bimaterial contrast enhances this penetration further as observed for the $r_c = 0.9$ and $r_c = 0.8$ cases. This is primarily attributed to higher reduction in normal stress in the direction of preferred propagation due to the increase in material contrast (as shown in Fig. 7a). For some combination of parameters, the rupture may penetrate through the entirety of the velocity strengthening patch. These observations imply that rupture penetration could be enhanced by either a reduction in the velocity strengthening frictional coefficients or an increase in the normal stress drop. The latter may be facilitated by an increase in material contrast or an increase in the propagation distance in the preferred direction (as shown in Fig. 7 and Fig. 6d).

This correlation may be deduced through estimating the resistance C of the VS patch to slipping, which was described by Kaneko et al. (2010) and defined as:

$$C = \sigma_{VS} \left(a_{VS} - \lambda^* b_{VS} \right) \ln \left(\frac{V_{dyn}}{V_i} \right) D_{VS}$$
 (18)

where, σ_{VS} is the effective normal stress in the velocity strengthening patch, D_{VS} is length of the VS patch, V_{dyn} , and V_i are the seismic and interseismic slip velocities on the VS patch. The parameter λ^* arises from the short lived stress increases at the rupture tip, and approaches one for small critical slip distance L. Thus, the approximate resistance of the VS patch to slipping depends on the normal stress distribution, as well as, the frictional

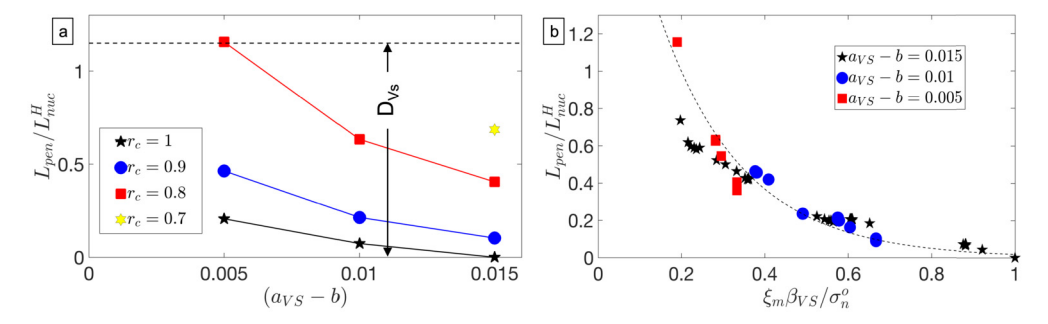


Fig. 9. Variation of the rupture propagation distance into the creeping region depending on the frictional properties and the material contrasts. (a) The length of the rupture penetration within the velocity strengthening patch, normalized by the nucleation size, for different bimaterial contrasts at different ($a_{VS} - b$) values, (b) the length of the rupture penetration within the velocity strengthening patch, normalized by the nucleation size, for different normal stress drops and frictional parameters. D_{VS} is the length of VS patch.

coefficients of the VS patch for a fixed D_{VS} and similar seismic slip velocities.

For a VS patch of a given length, the resistance to penetration can be attributed to either normal stress perturbations, or frictional coefficient changes or both. Utilizing the definition of the patch resistance we can then normalize the minimum normal stress during an earthquake event at the boundary of the velocity strengthening region by the initial normal stress. Furthermore, we introduce a non-dimensional parameter β_{VS} , defined as $\beta_{VS} = (a-b)/(a-b)_{max}$ on the VS patch, we note that the choice of $(a-b)_{max}$ is arbitrary and made such that the base case considered in our analysis showing no penetration, for the homogeneous case, corresponds to $\xi_m \beta_{VS}/\sigma_n^0=1$. This non-dimensional quantity $\xi_m \beta_{VS}/\sigma_n^0$ couples the effects of both normal stress perturbations and changes in the frictional parameters on rupture penetration. Fig. 9b shows that the rupture penetration is indeed correlated with the normalized normal stress for all the simulated earthquakes with variable normal stress changes and frictional properties. The results collapse nearly on a master curve shown in Fig. 8b. At lower values of $\xi_m \beta_{VS}/\sigma_n^0$ we observe that rupture penetration could grow unbounded within the VS patch. This suggests that for ruptures propagating on longer faults, the larger normal stress drops may cause destabilization of the entire length of the creeping patch.

5. Discussion

In this work, we consider a planar fault with a velocity weakening patch (VW) bordered by two velocity strengthening patches and separating two half spaces with dissimilar seismic velocities. We simulate sequences of earthquakes and aseismic slip in which we consider the full inertial and wave-mediated stress transfer during the dynamic rupture portion of the simulation. This enabled us to explore the effect of larger variations in the normal stress arising from the bimaterial coupling beyond what had been investigated earlier. Our results indicate that should the initial conditions on the fault be symmetric, the bimaterial coupling between slip and normal stress introduces heterogeneous stress conditions along the fault during aseismic slip. The heterogeneous stress distribution consequently results in a more favorable nucleation site and asymmetric rupture propagation.

The aseismic loading of the bimaterial interface introduces normal stress reduction accompanying the creeping front propagating in the theoretically preferred direction favoring rupture nucleation on one side (x > 0) of the fault. Accordingly, the rupture nucleation promotes propagation predominately in a preferred direction along the bimaterial interface. This leads to asymmetric rupture propagation, with higher slip rates, on one side of the fault, for the bimaterial versus homogeneous cases. This aligns with experimental results that show asymmetric rupture propagation along bimaterial

interfaces (Xia et al., 2004). Furthermore, we occasionally observe rupture nucleation in a non-favorable site, which propagates predominantly in a non-preferred direction, leading to smaller peak slip rates and lower slip accumulation. This implies that introducing material mismatch does not always guarantee preferred nucleation. Rather, other parameters, such as stress heterogeneity and, interestingly, frictional characteristics of the velocity strengthening patches, may influence the nucleation. Similar observations were reported in earlier work (Harris and Day, 2005, 2006; Kane et al., 2013; Rubin and Gillard, 2000). A distinct feature of our model is that stresses and seismicity co-evolve naturally over long time scales without imposing arbitrary stress distribution or forced nucleation as routinely done in simulations of single dynamic ruptures.

Through studying different material contrast we observed that rupture asymmetry is enhanced as the material contrast increase. This is mainly attributed to the increase in the normal stress drop which accompanies higher material contrast. Furthermore, changes to the nucleation site with increased material contrast favor longer rupture propagation in the preferred direction. Ruptures propagating in the preferred direction are accompanied by a tensile stress change, and thus achieve dynamic weakening that promotes higher slip rates. These observations are consistent with previous studies for dynamic rupture on a bimaterial interface, as well as, laboratory studies that show clear tendency for preferred propagation direction (Anooshehpoor and Brune, 1999). Along the same line our results are in agreement with field observations on rupture directivity of subduction zone earthquakes in Northern Chile which demonstrated a dominating rupture direction in downdip direction that could be attributed material contrast at the subduction interface (Folesky et al., 2018). It is important to note that while our observation of rupture directivity carries forward to natural systems, there are other factors that could further contribute to dominant rupture direction such as fault geometry, and accumulation off-fault damage.

As the dynamic weakening introduced by the bimaterial coupling increases with material contrast, we observe extended rupture propagation for similar frictional properties. This implies that the elastodynamic coupling introduced by the mismatch in material properties alters the frictional stability of the interface without introducing any changes to frictional parameters. Accordingly, we extended our investigation to incorporate the impact of different rate strengthening properties of the creeping patches that border the rate weakening portion of the fault. Our analysis revealed several interesting characteristics. For example, we demonstrate that while the properties of the velocity weakening patch remain similar, and for the same material contrast, we may achieve a higher degree of asymmetry by altering $(a_{VS} - b)$ distribution. A particularly important observation in this study is the interaction between dynamic weakening associated with normal stress perturbations in

the preferred propagation direction and the stability of the fault creeping segment. Since the resistance of the VS patch to unstable sliding is correlated to the normal stress on the patch, the extent of rupture penetration is similarly proportional to normal stress at the onset of penetration. Albeit due to a different mechanism, similar observations for large slip accumulation in velocity strengthening region due to substantial decrease in normal stress from geometrical effects have been also highlighted for dip-slip faults intersecting a free surface (Ryan and Oglesby, 2017; Kozdon and Dunham, 2013). Such penetration is particularly hazardous for cases with alternating locked and creeping segments and may lead to ruptures tunneling through energetically unfavorable (from the stand point of frictional strength at low slip rates) areas on a fault, and making it to a subsequent velocity-weakening zone on the other side, greatly extending the size of the potential earthquakes. Longer faults are more susceptible to this effect due to the potential for achieving larger dynamic normal stress changes as discussed earlier.

In all our simulations with the current framework utilizing a rate-and-state frictional law and the given fault dimension, we have only observed asymmetric crack-like rupture propagation. It remains to be investigated in future work whether other factors such as strong rate-weakening response or even larger normal stress drops could lead to the emergence of pulse-like ruptures. Furthermore, the nucleation mechanism for ruptures propagating on bimaterial interfaces plays an important role (Ben-Zion, 2006). Prior studies that observed pulse-like transitions for single dynamic rupture event relied primarily on artificial nucleation of rupture, however, nucleation in the current framework was driven by the aseismic creeping on the fault surface which could play a role in the generation of pulses (Ampuero and Ben-zion, 2008; Ben-Zion, 2001). Erickson and Day (2016) utilizing a rate-and-state frictional framework observed no pulse generation, however, the study was limited to quasi-dynamic analysis with small normal stress perturbations.

Our observations highlight the importance of incorporating inertial effects within earthquake cycle simulations of bimaterial interfaces. While several features, such as rupture preferred directionality and altered nucleation sites, agree with prior work within the quasi-dynamic approximation, the limited normal stress perturbations within the quasi-dynamic framework might lead to underestimating the potential hazard associated with fault slip on bimaterial interfaces (Erickson and Day, 2016). Specifically, the enhanced dynamic weakening observed during dynamic rupture which leads to larger dynamic stress drops and consequently larger slip velocities, is absent in the quasi-dynamic model. Furthermore, the larger normal stress drop observed in our dynamic simulations contributes significantly to the rupture penetration into the velocity strengthening patch which may have important implications for earthquake gates.

Here, we focused primarily on the role of frictional properties within the velocity strengthening patch while keeping other parameters fixed, it would be important to consider the interplay between frictional properties within the velocity weakening patch and the overall spatio-temporal characteristics of the earthquake sequence as well. While the choice of different frictional parameters within the velocity weakening would alter the earthquake cycle in terms of peak slip rate and inter-event time, we believe that the quantitative observations reported here, such as preferred directionality and enhanced dynamic weakening, will still be applicable. Furthermore, the apparently high dynamic stress drops in our simulations (\sim 30 MPa) are transient and the final static stress drops are much smaller (< 10 MPa). These high dynamic stress drops are manifestations of the strong dynamic weakening due to the normal stress-slip coupling on the bimaterial interface and are only weakly dependent on the frictional parameters. However, we recognize that the 2-D nature of the problem considered in our analysis introduces some approximations that could potentially lead to varying qualitative differences, and warrant further investigation in a 3-D setting. Furthermore, we have limited our investigation to modeling the sequence of earthquakes and aseismic slip in linear elastic domains. We recognize that the off-fault yielding provides an additional energy sink that may reduce the asymmetric behavior and decrease the large slip rates observed due to the bimaterial coupling as shown by (Duan, 2008; DeDontney et al., 2011b). This will be a focus of future work.

CRediT authorship contribution statement

Mohamed Abdelmeguid: Conception and design of study, Analysis of data, Drafting the manuscript. **Ahmed Elbanna:** Conception and design of study, Analysis of data, Drafting the manuscript.

Declaration of competing interest

The authors declare that they have no known competing financial interests or personal relationships that could have appeared to influence the work reported in this paper.

Availability of data and materials

The code and input files used in the study are available upon request.

Acknowledgement

We thank Yihe Huang and an anonymous reviewer for their insightful reviews that helped improve the manuscript. The authors acknowledge support from the Southern California Earthquake Center through a collaborative agreement between National Science Foundation. Grant Number: EAR0529922 and USGS. Grant Number: 07HQAG0008 and the National Science Foundation CAREER award No. 1753249 for modeling complex fault zone structures. This material is based upon work supported by the Department of Energy under Award Number DE-FE0031685.

References

Abdelmeguid, M., Ma, X., Elbanna, A., 2019. A novel hybrid finite element-spectral boundary integral scheme for modeling earthquake cycles: application to rate and state faults with low-velocity zones. J. Geophys. Res., Solid Earth 124 (12), 12854–12881. https://doi.org/10.1029/2019/B018036.

Adams, G.G., 1995. Self-excited oscillations of two elastic half-spaces sliding with a constant coefficient of friction. J. Appl. Mech. 62 (4), 867–872. https://doi.org/10.1115/1.2896013. https://asmedigitalcollection.asme.org/appliedmechanics/article/62/4/867/396221/SelfExcited-Oscillations-of-Two-Elastic-HalfSpaces.

Allam, A.A., Ben-Zion, Y., Kurzon, I., Vernon, F., 2014. Seismic velocity structure in the Hot Springs and Trifurcation areas of the San Jacinto fault zone, California, from double-difference tomography. Geophys. J. Int. 198 (2), 978–999. https://doi.org/10.1093/gji/ggu176.

Ampuero, J.-P., Rubin, A.M., 2008. Earthquake nucleation on rate and state faults – aging and slip laws. J. Geophys. Res. 113 (B1), B01302. https://doi.org/10.1029/2007JB005082. http://doi.wiley.com/10.1029/2007JB005082.

Ampuero, J.P., Ben-zion, Y., 2008. Cracks, pulses and macroscopic asymmetry of dynamic rupture on a bimaterial interface with velocity-weakening friction. Geophys. J. Int. 173 (2), 674–692. https://doi.org/10.1111/j.1365-246X.2008.03736.x.

Andrews, D.J., Ben-Zion, Y., 1997. Wrinkle-like slip pulse on a fault between different materials. J. Geophys. Res., Solid Earth 102 (B1), 553–571. https://doi.org/10. 1029/96jb02856.

Anooshehpoor, A., Brune, J.N., 1999. Wrinkle-like Weertman pulse at the interface between two blocks of foam rubber with different velocities. Geophys. Res. Lett. 26 (13), 2025–2028. https://doi.org/10.1029/1999GL900397.

Ben-Zion, Y., 2001. Dynamic ruptures in recent models of earthquake faults. Tech. Rep. www.elsevier.com/locate/jmps.

Ben-Zion, Y., 2006. Comment on "Material contrast does not predict earthquake rupture propagation direction" by R.A. Harris and S.M. Day. Geophys. Res. Lett. 33 (13). https://doi.org/10.1029/2005GL025652.

- Ben-Zion, Y., Malin, P., 1991. San Andreas fault zone head waves near Parkfield, California. Tech. Rep. 5001.
- Ben-Zion, Y., Shi, Z., 2005. Dynamic rupture on a material interface with spontaneous generation of plastic strain in the bulk, Earth Planet. Sci. Lett. 236 (1–2), 486–496. https://doi.org/10.1016/j.epsl.2005.03.025.
- Ben-Zion, Y., Katz, S., Leary, P., 1992. Joint inversion of fault zone head waves and direct P arrivals for crustal structure near major faults. J. Geophys. Res. 97 (B2), 1943–1951. https://doi.org/10.1029/91JB02748.
- Ben-Zion, Y., Peng, Z., Okaya, D., Seeber, L., Armbruster, J.G., Ozer, N., Michael, A.J., Baris, S., Aktar, M., 2003. A shallow fault-zone structure illuminated by trapped waves in the Karadere-Duzce branch of the North Anatolian Fault, western Turkey. Geophys. J. Int. 152 (3), 699–717. https://doi.org/10.1046/j.1365-246X.2003.01870.x. https://academic.oup.com/gji/article-lookup/doi/10.1046/j.1365-246X.2003.01870.x.
- Brietzke, G.B., Ben-Zion, Y., 2006. Examining tendencies of in-plane rupture to migrate to material interfaces. Geophys. J. Int. 167 (2), 807–819. https://doi.org/10.1111/j.1365-246X.2006.03137.x. https://academic.oup.com/gji/article-lookup/doi/10.1111/j.1365-246X.2006.03137.x.
- Cochard, A., Rice, J.R., 2000. Fault rupture between dissimilar materials: ill-posedness, regularization, and slip-pulse response. J. Geophys. Res., Solid Earth 105 (B11), 25891–25907. https://doi.org/10.1029/2000JB900230. http://doi.wiley.com/10.1029/2000JB900230.
- Dalguer, L.A., Day, S.M., 2009. Asymmetric rupture of large aspect-ratio faults at bimaterial interface in 3D. Geophys. Res. Lett. 36 (23), L23307. https://doi.org/10. 1029/2009GL040303. http://doi.wiley.com/10.1029/2009GL040303.
- Danesi, S., Bannister, S., Morelli, A., 2007. Repeating earthquakes from rupture of an asperity under an Antarctic outlet glacier. Earth Planet. Sci. Lett. 253 (1–2), 151–158. https://doi.org/10.1016/j.epsl.2006.10.023.
- DeDontney, N., Rice, J.R., Dmowska, R., 2011a. Influence of material contrast on fault branching behavior. Geophys. Res. Lett. 38 (14). https://doi.org/10.1029/ 2011GL047849. http://doi.wiley.com/10.1029/2011GL047849.
- DeDontney, N., Templeton-Barrett, E.L., Rice, J.R., Dmowska, R., 2011b. Influence of plastic deformation on bimaterial fault rupture directivity. J. Geophys. Res. 116 (B10), B10312. https://doi.org/10.1029/2011JB008417. http://doi.wiley.com/10. 1029/2011JB008417.
- Dieterich, J.H., 1979. Modeling of rock friction 1. Experimental results and constitutive equations. J. Geophys. Res., Solid Earth 84 (B5), 2161–2168. https://doi.org/10.1029/JB084iB05p02161.
- Dieterich, J.H., 1992. Earthquake nucleation on faults with rate- and state-dependent strength. Tectonophysics 211 (1-4), 115–134. https://doi.org/10.1016/0040-1951(92)90055-B.
- Dor, O., Rockwell, T.K., Ben-Zion, Y., 2006a. Geological observations of damage asymmetry in the structure of the San Jacinto, San Andreas and Punchbowl faults in Southern California: a possible indicator for preferred rupture propagation direction. Pure Appl. Geophys. 163 (2–3), 301–349. https://doi.org/10. 1007/s00024-005-0023-9.
- Dor, O., Ben-Zion, Y., Rockwell, T.K., Brune, J., 2006b. Pulverized rocks in the Mojave section of the San Andreas Fault Zone. Earth Planet. Sci. Lett. 245 (3-4), 642-654. https://doi.org/10.1016/j.epsl.2006.03.034.
- Duan, B., 2008. Asymmetric off-fault damage generated by bilateral ruptures along a bimaterial interface. Geophys. Res. Lett. 35 (14), L14306. https://doi.org/10.1029/ 2008GL034797. http://doi.wiley.com/10.1029/2008GL034797.
- Eberhart-Phillips, D., Michael, A.J., 1998. Seismotectonics of the Loma Prieta, California, region determined from three-dimensional Vp, Vp/Vs, and seismicity. J. Geophys. Res., Solid Earth 103 (9), 21099–21120. https://doi.org/10.1029/98jb01984.
- Erickson, B.A., Day, S.M., 2016. Bimaterial effects in an earthquake cycle model using rate-and-state friction. J. Geophys. Res., Solid Earth 121 (4), 2480–2506. https://doi.org/10.1002/2015JB012470.
- Erickson, B.A., Dunham, E.M., 2014. An efficient numerical method for earthquake cycles in heterogeneous media: alternating subbasin and surface-rupturing events on faults crossing a sedimentary basin. J. Geophys. Res., Solid Earth 119 (4), 3290–3316. https://doi.org/10.1002/2013JB010614.
- Folesky, J., Kummerow, J., Shapiro, S.A., 2018. Patterns of rupture directivity of subduction zone earthquakes in Northern Chile. J. Geophys. Res., Solid Earth 123 (12), 785–810. https://doi.org/10.1029/2018JB016331.
- Freund, L.B., 1979. The mechanics of dynamic shear crack propagation. J. Geophys. Res., Solid Earth 84 (B5), 2199–2209. https://doi.org/10.1029/JB084iB05p02199.
- Fuis, G.S., Clayton, R.W., Davis, P.M., Lutter, W.J., Okaya, D.A., Murphy, J.M., Benthien, M.L., Baher, S.A., Kohler, M.D., Simila, G., Keller, G.R., 2003. Fault systems of the 1971 San Fernando and 1994 Northridge earthquakes, southern California: relocated aftershocks and seismic images from LARSE II. Tech. rep. http://pubs.geoscienceworld.org/gsa/geology/article-pdf/31/2/171/3526634/i0091-7613-31-2-171.pdf.
- Geubelle, P.H., Breitenfeld, M.S., 1997. Numerical analysis of dynamic debonding under anti-plane shear loading. Int. J. Fract. 85 (3), 265–282. https://doi.org/10.1023/A:1007498300031.
- Harris, R.A., Day, S.M., 2005. Material contrast does not predict earthquake rupture propagation direction. Geophys. Res. Lett. 32 (23), 1–4. https://doi.org/10.1029/ 2005GL023941.

- Harris, R.A., Day, S.M., 2006. Reply to comment by Y. Ben-Zion on "Material contrast does not predict earthquake rupture propagation direction". Geophys. Res. Lett. 331 (13). https://doi.org/10.1029/2006GL026811.
- Henry, C., Das, S., 2001. Aftershock zones of large shallow earthquakes: fault dimensions, aftershock area expansion and scaling relations. Geophys. J. Int. 147 (2), 272–293. https://doi.org/10.1046/j.1365-246X.2001.00522.x.
- Herrendörfer, R., Gerya, T., van Dinther, Y., 2018. An invariant rate- and state-dependent friction formulation for viscoeastoplastic earthquake cycle simulations. J. Geophys. Res., Solid Earth 123 (6), 5018–5051. https://doi.org/10.1029/2017JB015225.
- Hutchinson, J., Suo, Z., 1991. Mixed Mode Cracking in Layered Materials. Academic Press, pp. 63–191. https://linkinghub.elsevier.com/retrieve/pii/ S0065215608701649
- Kane, D.L., Shearer, P.M., Goertz-Allmann, B.P., Vernon, F.L., 2013. Rupture directivity of small earthquakes at Parkfield. J. Geophys. Res., Solid Earth 118 (1), 212–221. https://doi.org/10.1029/2012/B009675.
- Kaneko, Y., Avouac, J.P., Lapusta, N., 2010. Towards inferring earthquake patterns from geodetic observations of interseismic coupling. Nat. Geosci. 3 (5), 363–369. https://doi.org/10.1038/ngeo843.
- Kozdon, J.E., Dunham, E.M., 2013. Rupture to the trench: dynamic rupture simulations of the 11 march 2011 Tohoku earthquake. Bull. Seismol. Soc. Am. 103 (2B), 1275–1289. https://doi.org/10.1785/0120120136.
- Lapusta, N., Rice, J.R., 2003. Nucleation and early seismic propagation of small and large events in a crustal earthquake model. J. Geophys. Res., Solid Earth 108 (B4), 1–18. https://doi.org/10.1029/2001JB000793. http://doi.wiley.com/10.1029/2001JB000793.
- Lapusta, N., Rice, J.R., Ben-Zion, Y., Zheng, G., 2000. Elastodynamic analysis for slow tectonic loading with spontaneous rupture episodes on faults with rate- and state-dependent friction. J. Geophys. Res., Solid Earth 105 (B10), 23765–23789. https://doi.org/10.1029/2000JB900250. http://doi.wiley.com/10. 1029/2000JB900250.
- Lewis, M.A., Ben-Zion, Y., 2010. Diversity of fault zone damage and trapping structures in the Parkfield section of the San Andreas Fault from comprehensive analysis of near fault seismograms. Geophys. J. Int. 183 (3), 1579–1595. https://doi.org/10.1111/j.1365-246X.2010.04816.x. https://academic.oup.com/gji/article-lookup/doi/10.1111/j.1365-246X.2010.04816.x.
- Liu, Y., Rice, J.R., 2007. Spontaneous and triggered aseismic deformation transients in a subduction fault model. J. Geophys. Res. 112 (B9), B09404. https://doi.org/ 10.1029/2007JB004930. http://doi.wiley.com/10.1029/2007JB004930.
- Lutter, W.J., 2004. Upper crustal structure from the Santa Monica Mountains to the Sierra Nevada, Southern California: tomographic results from the Los Angeles regional seismic experiment, Phase II (LARSE II). Bull. Seismol. Soc. Am. 94 (2), 619–632. https://doi.org/10.1785/0120030058. https://pubs.geoscienceworld.org/bssa/article/94/2/619-632/146953.
- Ma, X., Elbanna, A., 2019. Dynamic rupture propagation on fault planes with explicit representation of short branches. Earth Planet. Sci. Lett. 523, 115702. https://doi.org/10.1016/j.epsl.2019.07.005. https://linkinghub.elsevier. com/retrieve/pii/S0012821X19303887.
- Ma, X., Hajarolasvadi, S., Albertini, G., Kammer, D.S., Elbanna, A.E., 2018. A hybrid finite element-spectral boundary integral approach: applications to dynamic rupture modeling in unbounded domains. Int. J. Numer. Anal. Methods Geomech. 43 (1), 317–338. https://doi.org/10.1002/nag.2865. https://onlinelibrary.wiley.com/doi/abs/10.1002/nag.2865.
- McGuire, J., Ben-Zion, Y., 2005. High-resolution imaging of the Bear Valley section of the San Andreas fault at seismogenic depths with fault-zone head waves and relocated seismicity. Geophys. J. Int. 163 (1), 152–164. https://doi.org/10.1111/j. 1365-246X.2005.02703.x.
- McGuire, J.J., Zhao, L., Jordan, T.H., 2002. Predominance of unilateral rupture for a global catalog of large earthquakes. Tech. Rep. 8. http://pubs.geoscienceworld. org/ssa/bssa/article-pdf/92/8/3309/2717457/3309_928_01293.3309_3317.pdf.
- Price, S.P., Scott, B., 1994. Fault-block rotations at the edge of a zone of continental extension, southwest Turkey. J. Struct. Geol. 16 (3), 381–392. https://doi.org/10.1016/0191-8141(94)90042-6. https://linkinghub.elsevier.com/retrieve/pii/0191814194900426
- Ranjith, K., Rice, J.R., 2001. Slip dynamics at an interface between dissimilar materials. Tech. Rep. www.elsevier.com/locate/jmps.
- Rice, J.R., Ruina, A.L., 1983. Stability of steady frictional slipping. J. Appl. Mech. 50 (2), 343. https://doi.org/10.1115/1.3167042. http://appliedmechanics.asmedigitalcollection.asme.org/article.aspx?articleid=1406945.
- Rice, J.R., Lapusta, N., Ranjith, K., 2001. Rate and state dependent friction and the stability of sliding between elastically deformable solids. Tech. Rep. www. elsevier.com/locate/imps.
- Rubin, A.M., Ampuero, J.-P., 2007. Aftershock asymmetry on a bimaterial interface. J. Geophys. Res. 112 (B5), B05307. https://doi.org/10.1029/2006JB004337. http://doi.wiley.com/10.1029/2006JB004337.
- Rubin, A.M., Gillard, D., 2000. Aftershock asymmetry/rupture directivity among central San Andreas fault microearthquakes. J. Geophys. Res., Solid Earth 105 (B8), 19095–19109. https://doi.org/10.1029/2000jb900129.
- Ruina, A., 1983. Slip instability and state variable friction laws. J. Geophys. Res. 88 (B12), 10359–10370. https://doi.org/10.1029/[B088iB12p10359.

- Ryan, K.J., Oglesby, D.D., 2017. Modeling the effects of a normal-stress-dependent state variable, within the rate- and state-dependent friction framework, at stepovers and dip-slip faults. Pure Appl. Geophys. 174 (3), 1361–1383. https://doi.org/10.1007/s00024-017-1469-2.
- Shapiro, N.M., 2005. High-resolution surface-wave tomography from ambient seismic noise. Science 307 (5715), 1615–1618. https://doi.org/10.1126/science. 1108339. https://www.sciencemag.org/lookup/doi/10.1126/science.1108339.
- Shlomai, H., Fineberg, J., 2016. The structure of slip-pulses and supershear ruptures driving slip in bimaterial friction. Nat. Commun. 7 (1), 11787. https://doi.org/10.1038/ncomms11787. http://www.nature.com/articles/ncomms11787.
- Shlomai, H., Adda-Bedia, M., Arias, R.E., Fineberg, J., 2020. Supershear frictional ruptures along bimaterial interfaces. J. Geophys. Res., Solid Earth 125 (8). https://doi.org/10.1029/2020JB019829. https://onlinelibrary.wiley.com/doi/10.1029/2020JB019829.
- Takahashi, N., Kodaira, S., Nakanishi, A., Park, J.-O., Miura, S., Tsuru, T., Kaneda, Y., Suyehiro, K., Kinoshita, H., Hirata, N., Iwasaki, T., 2002. Seismic structure of western end of the Nankai trough seismogenic zone. J. Geophys. Res., Solid Earth 107 (B10), 1–2. https://doi.org/10.1029/2000jb000121.
- Tal, Y., Rubino, V., Rosakis, A.J., Lapusta, N., 2020. Illuminating the physics of dynamic friction through laboratory earthquakes on thrust faults. Proc. Natl. Acad. Sci. USA 117 (35), 21095–21100. https://doi.org/10.1073/pnas.2004590117. http://www.pnas.org/lookup/doi/10.1073/pnas.2004590117.

- Thomas, M.Y., Lapusta, N., Noda, H., Avouac, J.-P., 2014. Quasi-dynamic versus fully dynamic simulations of earthquakes and aseismic slip with and without enhanced coseismic weakening. J. Geophys. Res., Solid Earth 119 (3), 1986–2004. https://doi.org/10.1002/2013JB010615. http://doi.wiley.com/10.1002/2013JB010615.
- Thurber, C., Roecker, S., Zhang, H., Baher, S., Ellsworth, W., 2004. Fine-scale structure of the San Andreas fault zone and location of the SAFOD target earthquakes. Geophys. Res. Lett. 31 (12). https://doi.org/10.1029/2003gl019398.
- Wang, E., Rubin, A.M., 2011. Rupture directivity of microearthquakes on the San Andreas Fault from spectral ratio inversion. Geophys. J. Int. 186 (2), 852–866. https://doi.org/10.1111/j.1365-246X.2011.05087.x. https://academic.oup.com/gji/article-lookup/doi/10.1111/j.1365-246X.2011.05087.x.
- Weertman, J., 1980. Unstable slippage across a fault that separates elastic media of different elastic constants. J. Geophys. Res. 85 (B3), 1455–1461. https://doi.org/ 10.1029/JB085iB03p01455.
- Xia, K., Rosakis, A.J., Kanamori, H., 2004. Laboratory earthquakes: the sub-Rayleigh-to-supershear rupture transition. Science 303 (5665), 1859–1861. https://doi.org/10.1126/science.1094022. https://www.sciencemag.org/lookup/doi/10.1126/science.1094022.